INTERNATIONAL JOURNAL FOR NUMERICAL METHODS IN ENGINEERING
Int. J. Numer. Meth. Engng 2009; **77**:151–176
Published online 29 July 2008 in Wiley InterScience (www.interscience.wiley.com). DOI: 10.1002/nme.2397

Explicit finite element perfectly matched layer for transient three-dimensional elastic waves

Ushnish Basu*, †

Livermore Software Technology Corporation, Livermore, CA 94551, U.S.A.

SUMMARY

The use of a perfectly matched layer (PML) model is an efficient approach toward the bounded-domain modelling of wave propagation on unbounded domains. This paper formulates a three-dimensional PML for elastic waves by building upon previous work by the author and implements it in a displacement-based finite element setting. The novel contribution of this paper over the previous work is in making this finite element implementation suitable for explicit time integration, thus making it practicable for use in large-scale three-dimensional dynamic analyses. An efficient method of calculating the strain terms in the PML is developed in order to take advantage of the lack of the overhead of solving equations at each time step. The PML formulation is studied and validated first for a semi-infinite bar and then for the classical soil–structure interaction problems of a square flexible footing on a (i) half-space, (ii) layer on a half-space and (iii) layer on a rigid base. Numerical results for these problems demonstrate that the PML models produce highly accurate results with small bounded domains and at low computational cost and that these models are long-time stable, with critical time step sizes similar to those of corresponding fully elastic models. Copyright © 2008 John Wiley & Sons, Ltd.

Received 14 November 2007; Revised 5 May 2008; Accepted 10 May 2008

KEY WORDS: perfectly matched layers (PML); absorbing boundary; elastic waves; transient analysis; explicit integration; finite elements

1. INTRODUCTION

Modelling wave propagation on unbounded domains is crucial in many fields of science and engineering, and typically the complexity of the problem precludes analytical solutions and compels

*Correspondence to: Ushnish Basu, Livermore Software Technology Corporation, 7374 Las Positas Road, Livermore, CA 94551, U.S.A.
†E-mail: ubasu@lstc.com

Contract/grant sponsor: U.S. Bureau of Reclamation/Army Corps of Engineers; contract/grant number: W912HZ-05-P-0128
Contract/grant sponsor: San Diego Supercomputer Center/National Science Foundation: Academic Associates Program

a numerical approach [1, 2]. Of the many different numerical models for unbounded domains, local boundary conditions for absorbing outgoing waves [3–5] have often proved popular over rigorous non-local ones [6–9] because of their wider applicability, relative ease of implementation and low intrinsic computational cost, even if lower-order boundaries typically need an extended bounded domain to achieve a desired accuracy. For these reasons, recent research on local boundaries has flowed toward formulating practical higher-order boundaries that approach the accuracy of rigorous boundaries at a significantly lower computational cost [10–14].

An ideal absorbing boundary would be local in both space and time, computationally inexpensive, easy to implement, and of course robust and accurate. A promising candidate is the perfectly matched layer (PML) model, which was originally developed for electromagnetic waves [15, 16] and is now the method of choice for that community [17]. The PML approach is applicable to any linear wave equation [18] and PMLs have been formulated and studied for other wave equations [19–23] as well, including elastic waves [24–42]. It has been demonstrated that PMLs for elastic waves produce highly accurate results at low computational cost [35, 36].

A PML must be formulated with certain practical considerations in mind if it is to be widely adopted and used outside of in-house research software. Because of its intrinsic ability to model arbitrary and complex geometries and materials with relative ease, the finite element method [43–45] has become the method of choice for modelling solid mechanics and elasticity problems, and existing software for finite element modelling, analysis and visualization are predominantly geared toward the displacement-based finite element method. It is therefore pragmatic to formulate the PML in terms of displacement-based finite elements, because the object of interest in the analysis is not the PML itself, but what it bounds, which may be a domain with non-linear material and complex geometry [46, 47]; the PML merely serves to model the rest of the world [1]. Furthermore, it is imperative that the PML allows explicit time integration, because it is impractical to solve large systems of equations—from e.g. three-dimensional problems—at each time step. Most existing formulations of PMLs for transient elastic waves [24–30, 32–34, 37, 38, 40–42] use explicit time integration, but either with a finite-difference scheme or with a finite-difference-motivated split-field formulation in a finite element setting, with the split fields visible outside of the element.

The objective of this paper is to present a PML formulation and its displacement-based finite element implementation with explicit time integration for three-dimensional elastic waves. The formulation presented here extends previous work by the author [36], which developed a time-domain PML for two-dimensional elastic waves using displacement-based finite elements with implicit time integration, starting from a core frequency-domain PML [35] valid for both two- and three-dimensional elastic waves. The development parallels the one for the two-dimensional PML: the three-dimensional frequency-domain PML equations from Reference [35] are first transformed into the time domain by a special choice of the coordinate-stretching functions, and then these time-domain equations are made amenable to numerical solution by a straightforward finite element approach, with some special considerations for explicit integration. The viability of using explicit integration with PML is first investigated by studying (a) the effect of PML on the critical time step size, and (b) the effect of matrix lumping in the PML on the accuracy of results and on the critical time step size, in the context of a model semi-infinite bar. The PML formulation is then validated by modelling the classical soil–structure interaction problems of a square flexible footing on a (i) half-space, (ii) layer on a half-space and (iii) layer on a rigid base. This paper presents only a brief description of the concept of a PML because detailed development and derivations have been presented earlier [35, 36, 48].

DOI: 10.1002/nme

2. FORMULATION OF THE PML

2.1. Brief description

A PML (Figure 1) is a wave absorbing layer that, when placed adjacent to a truncated model of an unbounded domain, absorbs and attenuates all waves outgoing from it. The continuum PML is mathematically formulated—by applying a complex-valued coordinate stretching to the elastic wave equation—such that waves of all frequencies and all angles of incidence are absorbed into the PML without any reflection from the interface: the PML is thus 'perfectly matched' to the truncated domain. This novel property of the PML makes it fundamentally different from and more attractive than traditional local absorbing boundaries [3, 4] or layers [49, 50], even though it itself is a local formulation. Choosing a particular form of the coordinate stretch—in terms of an attenuation function—allows the PML to attenuate the wave inside the layer. The attenuated wave is reflected back toward the truncated domain from the outer boundary of the PML—which may be a fixed boundary—but the amplitude of the reflected wave re-entering the domain can be made arbitrarily small by appropriate choice of the attenuation function. Thus, any outgoing wave is only minimally reflected back, making the PML an appropriate model for the unbounded domain beyond.

2.2. Frequency-domain equations

Consider a homogeneous isotropic linear elastic medium undergoing small-strain dynamic motion in the absence of body forces. The displacements $\boldsymbol{u}(\boldsymbol{x}, t)$ of such a medium at point $\boldsymbol{x}$ and time t are governed by the following equations:

$$\operatorname{div}\boldsymbol{\sigma} = \rho\ddot{\boldsymbol{u}} \tag{1a}$$

$$\boldsymbol{\sigma} = \mathbf{C}\boldsymbol{\varepsilon} \tag{1b}$$

$$\boldsymbol{\varepsilon} = \tfrac{1}{2}[\operatorname{grad}\boldsymbol{u} + (\operatorname{grad}\boldsymbol{u})^{\mathrm{T}}] \tag{1c}$$

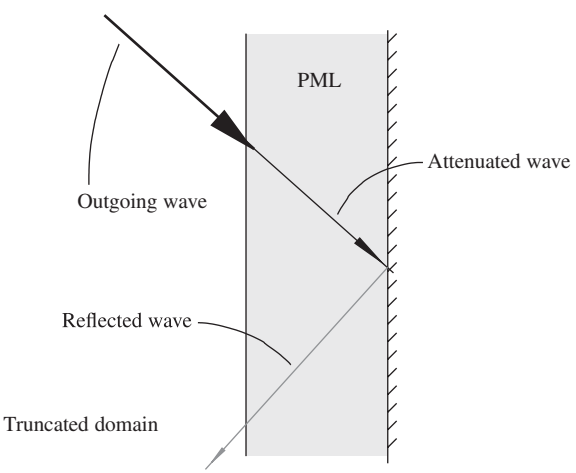

Figure 1. A PML adjacent to a truncated domain attenuates and reflects back an outgoing wave.

DOI: 10.1002/nme

where $\mathbf{C}$ is the elastic constitutive tensor, given in components C_{ijkl} by

$$\mathrm{C}_{ijkl} = (\kappa - \tfrac{2}{3}\mu)\delta_{ij}\delta_{kl} + \mu(\delta_{ik}\delta_{jl} + \delta_{il}\delta_{jk}) \tag{2}$$

with κ the bulk modulus and μ the shear modulus; ρ is the mass density of the medium, and $\boldsymbol{\sigma}$ and $\boldsymbol{\varepsilon}$ are the stress and infinitesimal strain tensors.

The corresponding PML medium is formulated naturally in the frequency domain, by assuming a harmonic time dependence of the displacement, stress and strain, e.g. $\boldsymbol{u}(\boldsymbol{x}, t) = \bar{\boldsymbol{u}}(\boldsymbol{x})\exp(\mathrm{i}\omega t)$, in Equation (1), where ω is the frequency of excitation. Let a three-dimensional space be defined by the coordinate system $\{x_i\}$, with respect to an orthonormal basis $\{\boldsymbol{e}_i\}$. For generality, we will consider a PML in which waves are attenuated along the coordinate axes $\{x_i'\}$, defined with respect to another orthonormal basis $\{\boldsymbol{e}_i'\}$. The governing frequency-domain equations for such a PML may be obtained by applying mutually independent nowhere-zero, continuous, complex-valued stretches λ_i to each of the coordinates $\{x_i'\}$, to obtain [35, 48]

$$\mathrm{div}(\bar{\boldsymbol{\sigma}}\mathscr{J}\boldsymbol{\Lambda}) = -\omega^2\rho\mathscr{J}\bar{\boldsymbol{u}} \tag{3a}$$

$$\bar{\boldsymbol{\sigma}} = \mathbf{C}\bar{\boldsymbol{\varepsilon}} \tag{3b}$$

$$\bar{\boldsymbol{\varepsilon}} = \tfrac{1}{2}[(\mathrm{grad}\,\bar{\boldsymbol{u}})\boldsymbol{\Lambda} + \boldsymbol{\Lambda}^{\mathrm{T}}(\mathrm{grad}\,\bar{\boldsymbol{u}})^{\mathrm{T}}] \tag{3c}$$

where

$$\mathscr{J} = \lambda_1(x_1')\lambda_2(x_2')\lambda_3(x_3'), \quad \boldsymbol{\Lambda}' = \mathrm{diag}(1/\lambda_1(x_1'), 1/\lambda_2(x_2'), 1/\lambda_3(x_3')) \tag{4}$$

and $\boldsymbol{\Lambda} = \mathbf{Q}\boldsymbol{\Lambda}'\mathbf{Q}^{\mathrm{T}}$, where $\mathbf{Q}$ is the rotation-of-basis matrix with components $Q_{ij} := \boldsymbol{e}_i \cdot \boldsymbol{e}_j'$. The above description of the PML uses the linear elastic constitutive law (Equation (3b)) for the sake of notational and algebraic simplicity, but in general, the PML can use any linear (visco-)elastic material model [18, 35, 36].

2.3. Time-domain equations

Equation (3) may be transformed into the time domain by choosing the stretching function to be of the form (no summation) [36]

$$\lambda_i(x_i') := [1 + f_i^{\mathrm{e}}(x_i')] - \mathrm{i}\frac{f_i^{\mathrm{p}}(x_i')}{a_0} \tag{5}$$

using a normalized frequency $a_0 = k_{\mathrm{s}}L$, where $k_{\mathrm{s}} = \omega/c_{\mathrm{s}}$ with c_{s} the shear wave speed and L is a characteristic length of the system; a convenient choice for L is the depth of the PML. The functions f_i^{e} in Equation (5) serve to attenuate evanescent waves, whereas the functions f_i^{p} serve to attenuate propagating waves. This choice of a coordinate stretch results in a simple dependence of Equation (3) on the factor $\mathrm{i}\omega$, thus allowing easy application of the inverse Fourier transform.

For this λ_i, the stretch tensor $\boldsymbol{\Lambda}$ can be expressed as

$$\boldsymbol{\Lambda} = \left[\mathbf{F}^{\mathrm{e}} + \frac{1}{\mathrm{i}\omega}\mathbf{F}^{\mathrm{p}}\right]^{-1} \tag{6}$$

where

$$\mathbf{F}^{\mathrm{e}} = \mathbf{Q}\mathbf{F}^{\mathrm{e}\prime}\mathbf{Q}^{\mathrm{T}}, \quad \mathbf{F}^{\mathrm{p}} = \mathbf{Q}\mathbf{F}^{\mathrm{p}\prime}\mathbf{Q}^{\mathrm{T}} \tag{7}$$

DOI: 10.1002/nme

with

$$\begin{aligned}\mathbf{F}^{\mathrm{e}\prime} &:= \mathrm{diag}(1+f_1^{\mathrm{e}}(x_1'),\, 1+f_2^{\mathrm{e}}(x_2'),\, 1+f_3^{\mathrm{e}}(x_3'))\\ \mathbf{F}^{\mathrm{p}\prime} &:= \mathrm{diag}(f_1^{\mathrm{p}}(x_1'),\, f_2^{\mathrm{p}}(x_2'),\, f_3^{\mathrm{p}}(x_3'))\times c_{\mathrm{s}}/L\end{aligned} \tag{8}$$

The product $\mathscr{J}\boldsymbol{\Lambda}$ can be expressed as

$$\mathscr{J}\boldsymbol{\Lambda} = \tilde{\mathbf{F}}^{\mathrm{ee}} + \frac{1}{\mathrm{i}\omega}\tilde{\mathbf{F}}^{\mathrm{ep}} - \frac{1}{\omega^2}\tilde{\mathbf{F}}^{\mathrm{pp}} \tag{9}$$

where

$$\tilde{\mathbf{F}}^{\mathrm{ee}} = \mathbf{Q}\tilde{\mathbf{F}}^{\mathrm{ee}\prime}\mathbf{Q}^{\mathrm{T}}, \quad \tilde{\mathbf{F}}^{\mathrm{ep}} = \mathbf{Q}\tilde{\mathbf{F}}^{\mathrm{ep}\prime}\mathbf{Q}^{\mathrm{T}}, \quad \tilde{\mathbf{F}}^{\mathrm{pp}} = \mathbf{Q}\tilde{\mathbf{F}}^{\mathrm{pp}\prime}\mathbf{Q}^{\mathrm{T}} \tag{10}$$

with

$$\begin{aligned}\tilde{\mathbf{F}}^{\mathrm{ee}\prime} &:= \mathrm{diag}(f_{23}^{\mathrm{ee}},\, f_{13}^{\mathrm{ee}},\, f_{12}^{\mathrm{ee}})\\ \tilde{\mathbf{F}}^{\mathrm{ep}\prime} &:= \mathrm{diag}(f_{23}^{\mathrm{ep}},\, f_{13}^{\mathrm{ep}},\, f_{12}^{\mathrm{ep}})\times c_s/L\\ \tilde{\mathbf{F}}^{\mathrm{pp}\prime} &:= \mathrm{diag}(f_{23}^{\mathrm{pp}},\, f_{13}^{\mathrm{pp}},\, f_{12}^{\mathrm{pp}})\times (c_{\mathrm{s}}/L)^2\end{aligned} \tag{11a}$$

where f_{ij}^{ee}, etc. are defined as (no summation)

$$\begin{aligned}f_{ij}^{\mathrm{ee}} &:= [1+f_i^{\mathrm{e}}(x_i')][1+f_j^{\mathrm{e}}(x_j')]\\ f_{ij}^{\mathrm{ep}} &:= [1+f_i^{\mathrm{e}}(x_i')]f_j^{\mathrm{p}}(x_j') + [1+f_j^{\mathrm{e}}(x_j')]f_i^{\mathrm{p}}(x_i')\\ f_{ij}^{\mathrm{pp}} &:= f_i^{\mathrm{p}}(x_i')f_j^{\mathrm{p}}(x_j')\end{aligned} \tag{11b}$$

Equation (3c) is pre-multiplied by $\mathrm{i}\omega\boldsymbol{\Lambda}^{-\mathrm{T}}$ and post-multiplied by $\boldsymbol{\Lambda}^{-1}$, Equations (5), (6) and (9) are substituted into Equation (3), and the inverse Fourier transform is applied to the resultant to obtain the time-domain equations for the three-dimensional elastic PML:

$$\mathrm{div}(\boldsymbol{\sigma}\tilde{\mathbf{F}}^{\mathrm{ee}} + \boldsymbol{\Sigma}\tilde{\mathbf{F}}^{\mathrm{ep}} + \tilde{\boldsymbol{\Sigma}}\tilde{\mathbf{F}}^{\mathrm{pp}}) = \rho f_{\mathrm{M}}\ddot{\boldsymbol{u}} + \rho\left(\frac{c_{\mathrm{s}}}{L}\right) f_{\mathrm{C}}\dot{\boldsymbol{u}} + \rho\left(\frac{c_{\mathrm{s}}}{L}\right)^2 f_{\mathrm{K}}\boldsymbol{u} + \rho\left(\frac{c_{\mathrm{s}}}{L}\right)^3 f_{\mathrm{H}}\boldsymbol{U} \tag{12a}$$

$$\boldsymbol{\sigma} = \mathbf{C}\boldsymbol{\varepsilon} \tag{12b}$$

$$\begin{aligned}&\mathbf{F}^{\mathrm{e}\mathrm{T}}\dot{\boldsymbol{\varepsilon}}\mathbf{F}^{\mathrm{e}} + (\mathbf{F}^{\mathrm{p}\mathrm{T}}\boldsymbol{\varepsilon}\mathbf{F}^{\mathrm{e}} + \mathbf{F}^{\mathrm{e}\mathrm{T}}\boldsymbol{\varepsilon}\mathbf{F}^{\mathrm{p}}) + \mathbf{F}^{\mathrm{p}\mathrm{T}}\mathbf{E}\mathbf{F}^{\mathrm{p}}\\ &\quad = \tfrac{1}{2}[\mathbf{F}^{\mathrm{e}\mathrm{T}}(\mathrm{grad}\,\dot{\boldsymbol{u}}) + (\mathrm{grad}\,\dot{\boldsymbol{u}})^{\mathrm{T}}\mathbf{F}^{\mathrm{e}}] + \tfrac{1}{2}[\mathbf{F}^{\mathrm{p}\mathrm{T}}(\mathrm{grad}\,\boldsymbol{u}) + (\mathrm{grad}\,\boldsymbol{u})^{\mathrm{T}}\mathbf{F}^{\mathrm{p}}]\end{aligned} \tag{12c}$$

where

$$\begin{aligned}f_{\mathrm{M}} &:= [1+f_1^{\mathrm{e}}(x_1')][1+f_2^{\mathrm{e}}(x_2')][1+f_3^{\mathrm{e}}(x_3')]\\ f_{\mathrm{C}} &:= [1+f_1^{\mathrm{e}}(x_1')][1+f_2^{\mathrm{e}}(x_2')]f_3^{\mathrm{p}}(x_3') + [1+f_1^{\mathrm{e}}(x_1')][1+f_3^{\mathrm{e}}(x_3')]f_2^{\mathrm{p}}(x_2')\\ &\quad + [1+f_2^{\mathrm{e}}(x_2')][1+f_3^{\mathrm{e}}(x_3')]f_1^{\mathrm{p}}(x_1')\\ f_{\mathrm{K}} &:= f_1^{\mathrm{p}}(x_1')f_2^{\mathrm{p}}(x_2')[1+f_3^{\mathrm{e}}(x_3')] + f_2^{\mathrm{p}}(x_2')f_3^{\mathrm{p}}(x_3')[1+f_1^{\mathrm{e}}(x_1')] + f_1^{\mathrm{p}}(x_1')f_3^{\mathrm{p}}(x_3')[1+f_2^{\mathrm{e}}(x_2')]\\ f_{\mathrm{H}} &:= f_1^{\mathrm{p}}(x_1')f_2^{\mathrm{p}}(x_2')f_3^{\mathrm{p}}(x_3')\end{aligned} \tag{13}$$

DOI: 10.1002/nme

and

$$\boldsymbol{U}:=\int_0^t \boldsymbol{u}\,\mathrm{d}\tau,\quad \mathbf{E}:=\int_0^t \boldsymbol{\varepsilon}\,\mathrm{d}\tau,\quad \boldsymbol{\Sigma}:=\int_0^t \boldsymbol{\sigma}\,\mathrm{d}\tau,\quad \tilde{\boldsymbol{\Sigma}}:=\int_0^t \boldsymbol{\Sigma}\,\mathrm{d}\tau \tag{14}$$

Application of the inverse Fourier transform to obtain $\boldsymbol{U}$, $\mathbf{E}$ and $\boldsymbol{\Sigma}$ assumes that $\bar{\boldsymbol{u}}(\omega=0)=0$, $\bar{\boldsymbol{\varepsilon}}(\omega=0)=0$, $\bar{\boldsymbol{\sigma}}(\omega=0)=0$. The presence of the time integrals of $\boldsymbol{\sigma}$ and $\boldsymbol{u}$ in the governing equations, although unconventional from the continuum mechanics point of view, is not unnatural in a time-domain implementation of a PML obtained without field splitting [51].

3. FINITE ELEMENT IMPLEMENTATION

3.1. Weak form

Equation (12) is implemented using a standard displacement-based finite element approach [45]. The weak form of Equation (12a) is derived by taking its inner product with an arbitrary weighting function $\boldsymbol{w}$ residing in an appropriate admissible space and then integrating over the entire PML domain Ω using integration by parts and the divergence theorem to obtain

$$\begin{aligned}&\int_\Omega \rho f_{\mathrm{M}}\boldsymbol{w}\cdot\ddot{\boldsymbol{u}}\,\mathrm{d}\Omega+\int_\Omega \rho\left(\frac{c_{\mathrm{s}}}{L}\right)f_{\mathrm{C}}\boldsymbol{w}\cdot\dot{\boldsymbol{u}}\,\mathrm{d}\Omega+\int_\Omega \rho\left(\frac{c_{\mathrm{s}}}{L}\right)^2 f_{\mathrm{K}}\boldsymbol{w}\cdot\boldsymbol{u}\,\mathrm{d}\Omega+\int_\Omega \rho\left(\frac{c_{\mathrm{s}}}{L}\right)^3 f_{\mathrm{H}}\boldsymbol{w}\cdot\boldsymbol{U}\,\mathrm{d}\Omega\\&\quad+\int_\Omega \tilde{\boldsymbol{\varepsilon}}^{\mathrm{ee}}:\boldsymbol{\sigma}\,\mathrm{d}\Omega+\int_\Omega \tilde{\boldsymbol{\varepsilon}}^{\mathrm{ep}}:\boldsymbol{\Sigma}\,\mathrm{d}\Omega+\int_\Omega \tilde{\boldsymbol{\varepsilon}}^{\mathrm{pp}}:\tilde{\boldsymbol{\Sigma}}\,\mathrm{d}\Omega=\int_\Gamma \boldsymbol{w}\cdot(\boldsymbol{\sigma}\tilde{\mathbf{F}}^{\mathrm{ee}}+\boldsymbol{\Sigma}\tilde{\mathbf{F}}^{\mathrm{ep}}+\tilde{\boldsymbol{\Sigma}}\tilde{\mathbf{F}}^{\mathrm{pp}})\boldsymbol{n}\,\mathrm{d}\Gamma\end{aligned} \tag{15}$$

where $\Gamma:=\partial\Omega$ is the boundary of Ω, and $\boldsymbol{n}$ is the unit outward normal to Γ. The symmetry of $\boldsymbol{\sigma}$ and $\boldsymbol{\Sigma}$ is used to obtain the last three integrals on the left-hand side, with

$$\begin{aligned}&\tilde{\boldsymbol{\varepsilon}}^{\mathrm{ee}}:=\tfrac{1}{2}[(\mathrm{grad}\,\boldsymbol{w})\tilde{\mathbf{F}}^{\mathrm{ee}}+\tilde{\mathbf{F}}^{\mathrm{ee}\mathrm{T}}(\mathrm{grad}\,\boldsymbol{w})^{\mathrm{T}}],\quad \tilde{\boldsymbol{\varepsilon}}^{\mathrm{ep}}:=\tfrac{1}{2}[(\mathrm{grad}\,\boldsymbol{w})\tilde{\mathbf{F}}^{\mathrm{ep}}+\tilde{\mathbf{F}}^{\mathrm{ep}\mathrm{T}}(\mathrm{grad}\,\boldsymbol{w})^{\mathrm{T}}]\\&\tilde{\boldsymbol{\varepsilon}}^{\mathrm{pp}}:=\tfrac{1}{2}[(\mathrm{grad}\,\boldsymbol{w})\tilde{\mathbf{F}}^{\mathrm{pp}}+\tilde{\mathbf{F}}^{\mathrm{pp}\mathrm{T}}(\mathrm{grad}\,\boldsymbol{w})^{\mathrm{T}}]\end{aligned} \tag{16}$$

3.2. System matrices and internal force

The weak form is first spatially discretized by interpolating $\boldsymbol{u}$ and $\boldsymbol{w}$ elementwise in terms of nodal quantities using appropriate nodal shape functions. This leads to the system of equations

$$\mathbf{m}\ddot{\boldsymbol{d}}+\mathbf{c}\dot{\boldsymbol{d}}+\mathbf{k}\boldsymbol{d}+\mathbf{K}\mathscr{D}+\boldsymbol{p}_{\mathrm{int}}=\boldsymbol{p}_{\mathrm{ext}} \tag{17}$$

where $\mathbf{m}$, $\mathbf{c}$ and $\mathbf{k}$ are, respectively, the mass, damping and stiffness matrices arising out of the inertial term on the right-hand side of Equation (3a), $\boldsymbol{d}$ is a vector of nodal displacements, $\mathscr{D}$ is given by

$$\mathscr{D}:=\int_0^t \boldsymbol{d}\,\mathrm{d}\tau \tag{18}$$

i.e. it is the vector of nodal values of $\boldsymbol{U}$ (cf. Equation (14a)); $\mathbf{K}$ is the coefficient matrix associated with $\mathscr{D}$ and also arising from the aforementioned inertial term; $\boldsymbol{p}_{\mathrm{int}}$ is a vector of internal force terms; and $\boldsymbol{p}_{\mathrm{ext}}$ is a vector of external forces.

DOI: 10.1002/nme

The inertial system matrices **m**, **c**, **k** and **K** may be assembled from their respective element-level constituent matrices:

$$\begin{aligned}\mathbf{m}^e &= \int_{\Omega^e} \rho f_{\mathrm{M}} \mathbf{N}^{\mathrm{T}}\mathbf{N}\,\mathrm{d}\Omega, \quad \mathbf{c}^e = \int_{\Omega^e} \rho \left(\frac{c_{\mathrm{s}}}{L}\right) f_{\mathrm{C}} \mathbf{N}^{\mathrm{T}}\mathbf{N}\,\mathrm{d}\Omega \\ \mathbf{k}^e &= \int_{\Omega^e} \rho \left(\frac{c_{\mathrm{s}}}{L}\right)^2 f_{\mathrm{K}} \mathbf{N}^{\mathrm{T}}\mathbf{N}\,\mathrm{d}\Omega, \quad \mathbf{K}^e = \int_{\Omega^e} \rho \left(\frac{c_{\mathrm{s}}}{L}\right)^3 f_{\mathrm{H}} \mathbf{N}^{\mathrm{T}}\mathbf{N}\,\mathrm{d}\Omega\end{aligned} \tag{19}$$

where **N** is the array of element-level nodal shape functions:

$$\mathbf{N} = [N_1\mathbf{I} \;\; N_2\mathbf{I} \;\; \cdots \;\; N_8\mathbf{I}] \tag{20}$$

e.g. for an 8-node brick, where **I** is the 3×3 identity matrix. However, for facilitating explicit time integration, these matrices are lumped by assigning to each diagonal entry the sum of all the entries in its row, to get

$$\begin{aligned}\mathbf{m}^e &= \int_{\Omega^e} \rho f_{\mathrm{M}} \mathbf{N}_d\,\mathrm{d}\Omega, \quad \mathbf{c}^e = \int_{\Omega^e} \rho \left(\frac{c_{\mathrm{s}}}{L}\right) f_{\mathrm{C}} \mathbf{N}_d\,\mathrm{d}\Omega \\ \mathbf{k}^e &= \int_{\Omega^e} \rho \left(\frac{c_{\mathrm{s}}}{L}\right)^2 f_{\mathrm{K}} \mathbf{N}_d\,\mathrm{d}\Omega, \quad \mathbf{K}^e = \int_{\Omega^e} \rho \left(\frac{c_{\mathrm{s}}}{L}\right)^3 f_{\mathrm{H}} \mathbf{N}_d\,\mathrm{d}\Omega\end{aligned} \tag{21}$$

where

$$\mathbf{N}_d = \mathrm{diag}(N_1\mathbf{1}, N_2\mathbf{1}, \ldots, N_8\mathbf{1}) \quad \text{with } \mathbf{1} := [1, 1, 1] \tag{22}$$

It is necessary to lump all the inertial matrices; lumping only the mass matrix, the minimum requirement for explicit integration, may lead to strong long-time instabilities in the system. To obtain a displacement-based formulation, the terms $\mathbf{c}\dot{\boldsymbol{d}}$, $\mathbf{k}\boldsymbol{d}$ and $\mathbf{K}\mathscr{D}$ in Equation (17) are computed at the element level using Equation (21), and then assembled into the global force vector.

The element-level internal force term is given by

$$\boldsymbol{p}^e_{\mathrm{int}} = \int_{\Omega^e} \tilde{\mathbf{B}}^{\mathrm{ee}\mathrm{T}} \hat{\boldsymbol{\sigma}}\,\mathrm{d}\Omega + \int_{\Omega^e} \tilde{\mathbf{B}}^{\mathrm{ep}\mathrm{T}} \hat{\boldsymbol{\Sigma}}\,\mathrm{d}\Omega + \int_{\Omega^e} \tilde{\mathbf{B}}^{\mathrm{pp}\mathrm{T}} \hat{\hat{\boldsymbol{\Sigma}}}\,\mathrm{d}\Omega \tag{23}$$

where $\tilde{\mathbf{B}}^{\mathrm{ee}}$ is given in terms of its nodal submatrices as

$$\tilde{\mathbf{B}}^{\mathrm{ee}}_I := \begin{bmatrix} \tilde{N}^{\mathrm{ee}}_{I1} & & \\ & \tilde{N}^{\mathrm{ee}}_{I2} & \\ & & \tilde{N}^{\mathrm{ee}}_{I3} \\ \tilde{N}^{\mathrm{ee}}_{I2} & \tilde{N}^{\mathrm{ee}}_{I1} & \\ \tilde{N}^{\mathrm{ee}}_{I3} & & \tilde{N}^{\mathrm{ee}}_{I1} \\ & \tilde{N}^{\mathrm{ee}}_{I3} & \tilde{N}^{\mathrm{ee}}_{I2} \end{bmatrix} \tag{24}$$

retaining the sparsity of the standard finite element compatibility matrix, and $\tilde{\mathbf{B}}^{\mathrm{ep}}$ and $\tilde{\mathbf{B}}^{\mathrm{pp}}$ are defined similarly, but with $\tilde{N}^{\mathrm{ee}}_{Ii}$ replaced by $\tilde{N}^{\mathrm{ep}}_{Ii}$ and $\tilde{N}^{\mathrm{pp}}_{Ii}$, respectively, where $\tilde{N}^{\mathrm{ee}}_{Ii}$, etc. are defined as

$$\tilde{N}^{\mathrm{ee}}_{Ii} := \tilde{F}^{\mathrm{ee}}_{ij} N_{I,j}, \quad \tilde{N}^{\mathrm{ep}}_{Ii} := \tilde{F}^{\mathrm{ep}}_{ij} N_{I,j}, \quad \tilde{N}^{\mathrm{pp}}_{Ii} := \tilde{F}^{\mathrm{pp}}_{ij} N_{I,j} \tag{25}$$

DOI: 10.1002/nme

Furthermore,

$$\hat{\boldsymbol{\sigma}} := \begin{Bmatrix} \sigma_{11} \\ \sigma_{22} \\ \sigma_{33} \\ \sigma_{12} \\ \sigma_{13} \\ \sigma_{23} \end{Bmatrix} \tag{26}$$

the vector form of $\boldsymbol{\sigma}$, with $\hat{\boldsymbol{\Sigma}}$ the time integral of $\hat{\boldsymbol{\sigma}}$, and $\hat{\hat{\boldsymbol{\Sigma}}}$ that of $\hat{\boldsymbol{\Sigma}}$. Because the PML is an unphysical medium, the symmetry of $\boldsymbol{\sigma}$, inherent in the representation in Equation (26), follows from the minor symmetry of $\mathbf{C}$, and not from the balance of angular momentum. The attenuation functions f_i^{e} and f_i^{p} are defined globally on the PML domain, not elementwise. It is conveniently assumed that there is no contribution to $\boldsymbol{p}_{\mathrm{ext}}$ from a free boundary of the PML.

The element integrals in Equations (21) and (23) are computed using an eight-point Gauss quadrature [45]. The possibility of reducing computational cost by using a single-point quadrature with hourglass control [44] has been explored in recent work [41], with the hourglass modes of an elastic element being used as hourglass modes for the PML element. A rational approach would likely prove difficult, because the PML system is intrinsically a non-classically damped system, and the stiffness and damping matrices of each element are unsymmetric and depend on its position as well as on the time step [36].

3.3. Time discretization

Integration of the equations of motion (Equation (17)) using the central-difference explicit scheme requires calculation of the total internal force at time t_n, assuming that the displacements have been calculated at time t_n and velocities at time $t_{n-1/2}$ [44].

The time integral of the displacement $\mathscr{D}$ is discretized as

$$\mathscr{D}_n = \mathscr{D}_{n-1} + \boldsymbol{d}_n \Delta t \tag{27}$$

where $\Delta t = t_n - t_{n-1}$. Note that $\mathscr{D}$ is required only where $\mathbf{K}^e \neq \mathbf{0}$, i.e. from Equation (21), wherever $f_{\mathrm{H}} \neq 0$. From Equation (13), it can be seen that this holds only in the corner regions of the PML, where waves are attenuated in all three coordinate directions. Thus, $\mathscr{D}_n$ needs to be stored and updated only in the corner regions.

The element-level internal force term $\boldsymbol{p}^e_{\mathrm{int},n}$ may be computed from $\hat{\boldsymbol{\sigma}}_n$, $\hat{\boldsymbol{\Sigma}}_n$ and $\hat{\hat{\boldsymbol{\Sigma}}}_n$ using Equation (23), with

$$\hat{\boldsymbol{\Sigma}}_n = \hat{\boldsymbol{\Sigma}}_{n-1} + \hat{\boldsymbol{\sigma}}_n \Delta t, \quad \hat{\hat{\boldsymbol{\Sigma}}}_n = \hat{\hat{\boldsymbol{\Sigma}}}_{n-1} + \hat{\boldsymbol{\Sigma}}_n \Delta t \tag{28}$$

where $\hat{\boldsymbol{\sigma}}_n$ is computed using Equation (12b) as

$$\hat{\boldsymbol{\sigma}}_n = \mathbf{D}\hat{\boldsymbol{\varepsilon}}_n \tag{29}$$

DOI: 10.1002/nme

with

$$\mathbf{D}:=\begin{bmatrix} \kappa+4\mu/3 & \kappa-2\mu/3 & \kappa-2\mu/3 & & & \\ \kappa-2\mu/3 & \kappa+4\mu/3 & \kappa-2\mu/3 & & & \\ \kappa-2\mu/3 & \kappa-2\mu/3 & \kappa+4\mu/3 & & & \\ & & & \mu & & \\ & & & & \mu & \\ & & & & & \mu \end{bmatrix}, \quad \hat{\boldsymbol{\varepsilon}}:=\begin{Bmatrix} \varepsilon_{11} \\ \varepsilon_{22} \\ \varepsilon_{33} \\ 2\varepsilon_{12} \\ 2\varepsilon_{13} \\ 2\varepsilon_{23} \end{Bmatrix}$$

where $\hat{\boldsymbol{\varepsilon}}_n$, the vector form of $\boldsymbol{\varepsilon}_n$, is to be computed from a time discretization of Equation (12c), as discussed in the following section.

3.4. Efficient computation of strain terms

Because an explicit time integration scheme does not have the overhead of solving a system of equations, it is crucial to compute the internal force as efficiently as possible. Toward this goal, the strain terms are computed from Equation (12c) by transforming into the PML basis $\{\boldsymbol{e}'_i\}$, which diagonalizes matrices $\mathbf{F}^{\mathrm{e}}$ and $\mathbf{F}^{\mathrm{p}}$. The approximations

$$\dot{\boldsymbol{\varepsilon}}(t_n)\approx\frac{\boldsymbol{\varepsilon}_n-\boldsymbol{\varepsilon}_{n-1}}{\Delta t}, \quad \mathbf{E}(t_n)\approx\mathbf{E}_{n-1}+\boldsymbol{\varepsilon}_n\Delta t \tag{30}$$

are used in Equation (12c) to obtain

$$\begin{aligned}\boldsymbol{\varepsilon}_n\Delta t=&\frac{1}{2}[\mathbf{F}^{\epsilon\mathrm{T}}(\mathrm{grad}\,\dot{\boldsymbol{u}}|_{n-1/2})\mathbf{F}^{\iota}+\mathbf{F}^{\iota\mathrm{T}}(\mathrm{grad}\,\dot{\boldsymbol{u}}|_{n-1/2})^{\mathrm{T}}\mathbf{F}^{\epsilon}]\\&+\frac{1}{2}[\mathbf{F}^{\varrho\mathrm{T}}(\mathrm{grad}\,\boldsymbol{u}_n)\mathbf{F}^{\iota}+\mathbf{F}^{\iota\mathrm{T}}(\mathrm{grad}\,\boldsymbol{u}_n)^{\mathrm{T}}\mathbf{F}^{\varrho}]+\frac{1}{\Delta t}\mathbf{F}^{\epsilon\mathrm{T}}\boldsymbol{\varepsilon}_{n-1}\mathbf{F}^{\epsilon}-\mathbf{F}^{\varrho\mathrm{T}}\mathbf{E}_{n-1}\mathbf{F}^{\varrho}\end{aligned} \tag{31}$$

where

$$\mathbf{F}^{\iota}:=\left[\frac{\mathbf{F}^{\mathrm{e}}}{\Delta t}+\mathbf{F}^{\mathrm{p}}\right]^{-1}, \quad \mathbf{F}^{\epsilon}:=\mathbf{F}^{\mathrm{e}}\mathbf{F}^{\iota}, \quad \mathbf{F}^{\varrho}:=\mathbf{F}^{\mathrm{p}}\mathbf{F}^{\iota} \tag{32}$$

Transforming Equation (31) into the PML basis $\{\boldsymbol{e}'_i\}$ gives

$$\begin{aligned}\boldsymbol{\varepsilon}'_n\Delta t=&\frac{1}{2}[\mathbf{F}^{\epsilon\prime}\mathbf{Q}^{\mathrm{T}}(\mathrm{grad}\,\dot{\boldsymbol{u}}|_{n-1/2})\mathbf{Q}\mathbf{F}^{\iota\prime}+\mathbf{F}^{\iota\prime}\mathbf{Q}^{\mathrm{T}}(\mathrm{grad}\,\dot{\boldsymbol{u}}|_{n-1/2})^{\mathrm{T}}\mathbf{Q}\mathbf{F}^{\epsilon\prime}]\\&+\frac{1}{2}[\mathbf{F}^{\varrho\prime}\mathbf{Q}^{\mathrm{T}}(\mathrm{grad}\,\boldsymbol{u}_n)\mathbf{Q}\mathbf{F}^{\iota\prime}+\mathbf{F}^{\iota\prime}\mathbf{Q}^{\mathrm{T}}(\mathrm{grad}\,\boldsymbol{u}_n)^{\mathrm{T}}\mathbf{Q}\mathbf{F}^{\varrho\prime}]\\&+\frac{1}{\Delta t}\mathbf{F}^{\epsilon\prime}\boldsymbol{\varepsilon}'_{n-1}\mathbf{F}^{\epsilon\prime}-\mathbf{F}^{\varrho\prime}\mathbf{E}'_{n-1}\mathbf{F}^{\varrho\prime}\end{aligned} \tag{33}$$

where the primed tensors are given by, e.g. $\boldsymbol{\varepsilon}'_n=\mathbf{Q}^{\mathrm{T}}\boldsymbol{\varepsilon}_n\mathbf{Q}$. Note that tensors $\mathbf{F}^{\epsilon\prime}$, $\mathbf{F}^{\varrho\prime}$ and $\mathbf{F}^{\iota\prime}$ are diagonal tensors.

The quantity $\mathbf{Q}^{\mathrm{T}}(\mathrm{grad}\,\boldsymbol{u})\mathbf{Q}$ in Equation (33)—dropping the time step subscript for ease of notation—is in fact the displacement gradient in the PML basis, which can be checked by computing

DOI: 10.1002/nme

it using indices: if the displacement $\boldsymbol{u}$ is interpolated as $u_k = N_I d_k^I$, where N_I is the shape function value for node I, and d_k^I is the displacement of node I in the direction $\boldsymbol{e}_i$, then

$$\mathbf{Q}^{\mathrm{T}}(\mathrm{grad}\,\boldsymbol{u})\mathbf{Q} \equiv u'_{i,j} = d_i^{I\prime} N'_{I,j} \quad \text{with } d_i^{I\prime} := Q_{ki} d_k^I, \quad N'_{I,j} := Q_{lj} N_{I,l} \tag{34}$$

where $d_i^{I\prime}$ is the displacement in the direction $\boldsymbol{e}'_i$ at node I, obtained by transforming d_k^I into the PML basis and $N'_{I,j}$ is the gradient of N_I in the direction $\boldsymbol{e}'_j$.

Upon rewriting the velocity terms in Equation (33) in a similar manner, $\boldsymbol{\varepsilon}'_n$ may be obtained in components as (no summation)

$$\begin{aligned}(\varepsilon'_{ij}|_n)\Delta t = {} & \frac{1}{2}[F_i^{\epsilon\prime}(v'_{i,j}|_{n-1/2})F_j^{\iota\prime} + F_i^{\iota\prime}(v'_{j,i}|_{n-1/2})F_j^{\epsilon\prime}] \\ & + \frac{1}{2}[F_i^{\varrho\prime}(u'_{i,j}|_n)F_j^{\iota\prime} + F_i^{\iota\prime}(u'_{j,i}|_n)F_j^{\varrho\prime}] \\ & + \frac{1}{\Delta t}F_i^{\epsilon\prime}(\varepsilon'_{ij}|_{n-1})F_j^{\epsilon\prime} - F_i^{\varrho\prime}(E'_{ij}|_{n-1})F_j^{\varrho\prime}\end{aligned} \tag{35}$$

where $v'_{i,j}$ is the velocity gradient in the PML basis; $F_i^{\epsilon\prime}$ is the ith diagonal element of $\mathbf{F}^{\epsilon\prime}$, and similarly for $F_i^{\varrho\prime}$ and $F_i^{\iota\prime}$. The strain $\boldsymbol{\varepsilon}_n$ in the global coordinates may be obtained by transforming $\boldsymbol{\varepsilon}'_n$ back:

$$\boldsymbol{\varepsilon}_n = \mathbf{Q}\boldsymbol{\varepsilon}'_n\mathbf{Q}^{\mathrm{T}} \tag{36}$$

3.5. Summary of element calculations

This profusion of equations above is summarized below in an element algorithm.

Initial mass computation. Compute the diagonal element mass matrix $\mathbf{m}^e$ using Equation (21), with f_{M} defined in Equation (13), and assemble into the global mass matrix.

Element force computation. Compute the internal element force $\boldsymbol{p}^e_{\mathrm{int},n}$ at time step t_n as follows:

1. Compute displacement and velocity gradients in the PML basis using Equation (34).
2. Compute the strain $\boldsymbol{\varepsilon}'_n$ in the PML basis using Equation (35) and transform to global coordinates using Equation (36).
3. Compute the stress $\hat{\boldsymbol{\sigma}}_n$ using Equation (29), and the stress time integrals $\hat{\boldsymbol{\Sigma}}_n$ and $\hat{\hat{\boldsymbol{\Sigma}}}_n$ from Equation (28).
4. Compute the internal force $\boldsymbol{p}^e_{\mathrm{int},n}$ using Equation (23).

Compute the total internal force as follows:

1. Compute the diagonal matrices $\mathbf{c}^e$, $\mathbf{k}^e$, $\mathbf{K}^e$ using Equation (21), with f_{C}, f_{K} and f_{H} given by Equation (13). Matrix $\mathbf{K}^e$ is computed only in the corner regions of the PML model.
2. In the corner regions of the model, compute the time integral of displacement $\mathscr{D}_n$ using Equation (27).
3. Add the force term (Equation (17))

$$\mathbf{c}^e\dot{\boldsymbol{d}}_{n-1/2} + \mathbf{k}^e\boldsymbol{d}_n + \mathbf{K}^e\mathscr{D}_n$$

to $\boldsymbol{p}^e_{\mathrm{int},n}$ to get the total internal force. The last term in the above expression is non-zero only in the corner regions of the PML model.

DOI: 10.1002/nme

4. EVALUATION OF EXPLICIT INTEGRATION WITH PML

In order to successfully use an explicit integration scheme with the PML model, two key issues need to be evaluated: (a) the effect of PML on the critical time step size and (b) the effect of lumping of the PML matrices in Equation (19) on the accuracy of results. Additionally, we can also evaluate the effect of lumping on the critical time step size. Because the complexity of the PML equations precludes an analytical evaluation in this paper, we resort to a numerical evaluation in the context of a bar of brick elements, which is analogous to the one-dimensional systems commonly used in the analytical evaluation of stability and accuracy.

Consider a semi-infinite elastic bar with a square cross section of width b (Figure 2(a)), with shear modulus μ, mass density ρ and the Poisson ratio ν, subjected to a uniform force at the free end. The time-domain response of this system is studied by applying the force either longitudinally along the axis of the bar—thus simulating P-waves—or transverse to it, thus simulating S-waves, and recording the displacement of the tip in the corresponding direction. In the latter case, the displacements of the bar along its axis are constrained in order to eliminate the beam bending modes, which are not supported by the PML model. The time variation of the force is given by a time-limited cosine wave bookended by cosine half-cycles and is characterized by its duration t_{d} and its dominant forcing frequency ω_{f}. A typical waveform and its Fourier transform are shown in Figure 3, and a detailed description of the waveform is given in Reference [36].

This bar is modelled using the PML model shown in Figure 2(b), discretized using eight-noded bricks, with one element across the cross section of the bar, and enough elements along the length of bar to adequately model the wave propagation, thus evoking a one-dimensional system. The attenuation functions within the PML (cf. Equation (5)) are chosen as $f_1^{\mathrm{e}} = f_1^{\mathrm{p}} = f_1$, and $f_2^{\mathrm{e}} = f_2^{\mathrm{p}} = f_3^{\mathrm{e}} = f_3^{\mathrm{p}} \equiv 0$, with f_1 chosen as [35, 36]

$$f_1(x_1) := f_0\left(\frac{x_1 - L_e}{L_P}\right) \tag{37}$$

An extended mesh model—fully elastic and extending up to $25b$ from the free end, with the same mesh density as the PML model—is used to provide benchmark results for assessing the accuracy of the results from the PML model.

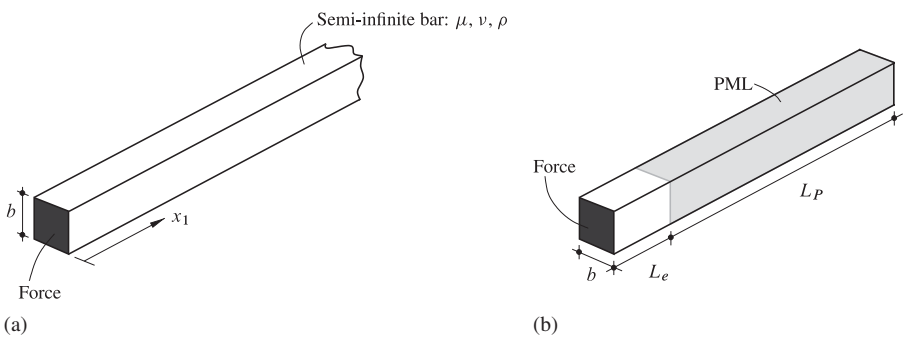

Figure 2. (a) Semi-infinite elastic bar subjected to a uniform force at the free end and (b) a PML model fixed at the outer boundary.

DOI: 10.1002/nme

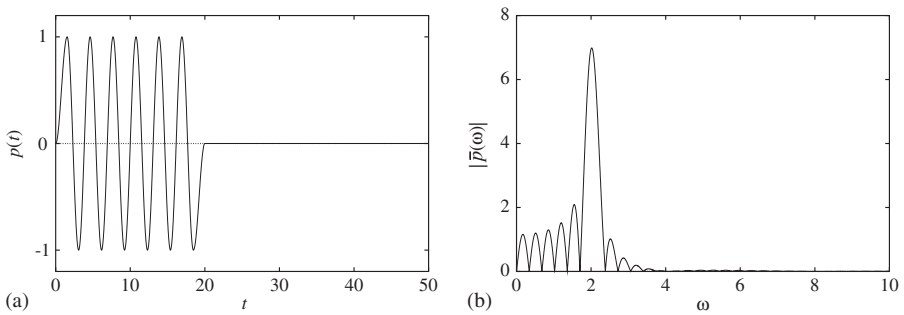

Figure 3. Plot of typical (a) applied force $p(t)$ with $t_d = 20$ and (b) amplitude of its Fourier transform $\bar{p}(\omega)$, with $\omega_f = 2$.

Table I. Comparison of critical time step sizes for three choices of lumping of inertial matrices in the PML model of a semi-infinite bar: $b = 0.1$; $L_e = 0.2$, $L_P = 0.8$; $f_0 = 10$; $t_d = 10$, $\omega_f = 3.0$.

	Lumped		Consistent		Intermediate	
Model	Longitudinal	Transverse	Longitudinal	Transverse	Longitudinal	Transverse
Elastic	0.04865	0.05009	0.02582	0.02586	—	
PML	0.04871	0.04921	0.02606	0.02632	Unstable	0.04958

The effect of the PML on the critical time step size is considered first by comparing the critical time step size of the PML model with that of a fully elastic model of the same size, i.e. one where the PML elements have been replaced with elastic elements. The critical time step size for either model is determined by carrying out the analysis with different time step sizes and converging upon the maximum step size for which we get stable results. Three variants of the PML model are considered: (a) all inertial matrices lumped (Equation (21)), (b) all inertial matrices consistent (Equation (19)) and (c) an intermediate formulation where only the mass matrix is lumped and the other inertial matrices are consistent.

Table I shows the critical time step sizes for both the elastic and the PML models, for both lumped and consistent matrices, as well as for the intermediate formulation for the PML. It is seen that for both the lumped and the consistent formulations, the critical time step size required by the PML model is approximately equal to that of the elastic model. The critical time step required for the intermediate formulation under transverse excitation is also similar to that required for the lumped formulation. However, for longitudinal excitation, the intermediate formulation exhibits a strong long-time instability in the free-vibration phase irrespective of the time step size.

This demonstrates that PML elements with either fully lumped or fully consistent matrices do not have any significant effect on the critical time step size for the corresponding elastic model. Furthermore, the PML elements exhibit behavior well known for elastic elements: consistent matrices yield smaller critical time step sizes than do lumped matrices [45]. This observation allows the speculation that for the intermediate formulation under longitudinal excitation—where the bar is unconstrained except at one end—the specific combination of lumped and consistent matrices reduces the critical time step size to an unreasonably small value. The longitudinal constraint

DOI: 10.1002/nme

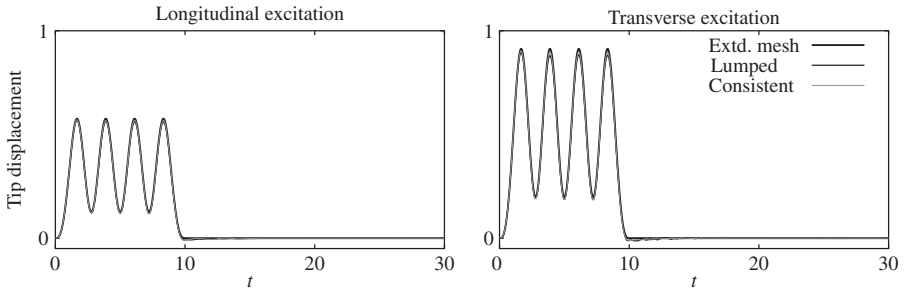

Figure 4. Tip displacements of a semi-infinite bar due to applied forces: longitudinal displacements due to longitudinal excitation; transverse displacements due to transverse excitation; $b=0.1$; $L_e=0.2$, $L_P=0.8$; $f_0=10$; $t_\mathrm{d}=10$, $\omega_\mathrm{f}=3.0$.

Table II. Comparison of relative error in tip displacement of PML model of a semi-infinite bar from consistent and lumped formulations: $b=0.1$; $L_e=0.2$, $L_P=0.8$; $f_0=10$; $t_\mathrm{d}=10$, $\omega_\mathrm{f}=3.0$.

	Longitudinal		Transverse	
	Lumped	Consistent	Lumped	Consistent
% error	2.89	1.73	3.71	2.24

imposed upon the bar for transverse excitation allows a stable solution for the intermediate formulation.

The effect of lumping on the accuracy of results is considered next. The error in the PML solution is computed relative to the benchmark extended mesh solution as

$$\%\ \text{error} := \frac{\max_n |\boldsymbol{u}_p(t_n) - \boldsymbol{u}_e(t_n)|}{\max_n |\boldsymbol{u}_e(t_n)|} \times 100 \tag{38}$$

where $\boldsymbol{u}_e$ and $\boldsymbol{u}_p$ are the tip displacements of the extended mesh model and the PML model, respectively, at time steps t_n. Figure 4 compares the displacements from the consistent and the lumped formulations of the PML with those from the extended mesh, for both longitudinal and transverse excitations, and Table II shows the errors from the two formulations.

It is difficult to visually distinguish the results from the two PML models, and both follow the extended mesh result closely. The computed errors from the lumped formulation are seen to be slightly larger than those from the consistent formulation, thus appearing to contradict analyses for elastic elements that posit that lumped masses are well matched with explicit integration, and are likely to produce more accurate results than consistent masses [45, 52]. It must be remarked that the error is characterized differently in the two cases: these classical studies of well-matched methods study the error in the natural frequency of the discrete system, whereas here the amplitude error is used to assess accuracy. However, because the difference in accuracy of the two formulations is negligible in practice, it is felt that this discrepancy with earlier analyses does not warrant further investigation.

DOI: 10.1002/nme

5. NUMERICAL RESULTS

Numerical results are presented for the classical soil–structure interaction problems of a square flexible footing on a (i) half-space, (ii) layer on a half-space and (iii) layer on a rigid base.

Figure 5(a) shows a quarter model of a homogeneous isotropic elastic half-space with shear modulus μ, mass density ρ and the Poisson ratio ν, subjected to a uniform force applied over a square area of half-width b. The time-domain response of this system is studied by applying the force either vertically or horizontally and recording the displacements in the corresponding direction at the center and at the corner of the square. The time variation of the force is of the form shown in Figure 3, characterized by its duration t_d and its dominant forcing frequency ω_f [36].

This unbounded domain system is modelled using the PML model shown in Figure 5(b), discretized using an adequately dense regular mesh of eight-noded bricks. For comparison, the half-space is also modelled using viscous dashpots [3], wherein the entire domain including the PML region is taken to be elastic and consistent dashpot elements replace the fixed outer boundary; thus, the mesh used for the dashpot model is comparable to that used for the PML model. An extended mesh model, composed entirely of elastic elements in the interior and with the same mesh density as the PML and the dashpot models, is used to provide benchmark results. This mesh extends to a distance of $25b$ downward from the center of the excitation, and laterally to a distance of $20b$ for vertical excitation and $25b$ for horizontal excitation; the dimensions are chosen to ensure that waves reflected back from the outer boundary—modelled using viscous dashpots—do not affect the recorded displacements within the duration of the simulation.

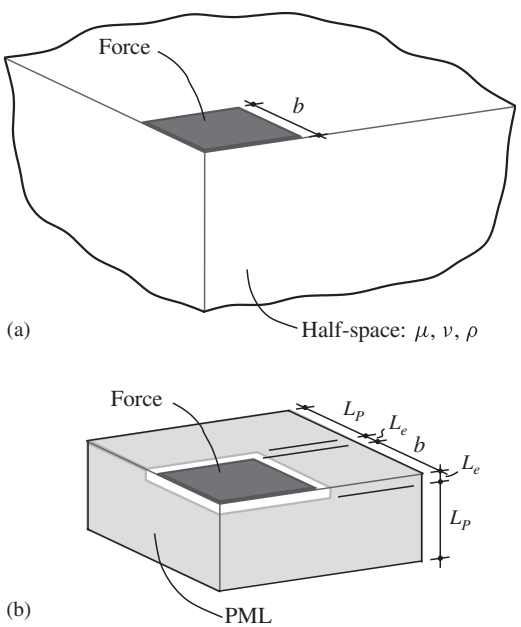

Figure 5. (a) Quarter model of a half-space subjected to a uniform force applied over a square area of half-width b and (b) a PML model fixed at the outer boundary.

DOI: 10.1002/nme

The attenuation functions in the PML (cf. Equation (5)) are chosen as $f_i^{\mathrm{e}} = f_i^{\mathrm{p}} = f_i$, with f_i now chosen to be a monomial:

$$f_i(x_i) := f_{0i}\left(\frac{x_i}{L_{Pi}}\right)^{\mathrm{p}} \quad \text{(no summation)} \tag{39}$$

where x_i is the distance into the PML, and L_{Pi} is the depth of the PML, in the ith direction. A quadratic monomial ($p=2$) is typically recommended because, in general, it is expected to best ameliorate the error due to the finite element discretization [48, 53]; this is in contrast to a continuum PML, where a linear monomial is optimal [35].

An optimal value of the coefficient f_{0i} may be estimated from a wave-reflection analysis of a discretized one-dimensional time-harmonic PML [48], by minimizing the expected reflection coefficient for a white-noise excitation. This work adopts an approach that is similar in spirit, but more directly applicable to three-dimensional problems: the optimal value of f_{0i} for a given PML depth—represented by the number of elements through the depth—for both $p=1$ and $p=2$, is found by minimizing the expected error in the response of a canonical three-dimensional PML model over a range of values of f_{0i}. The canonical PML model is chosen to be the half-space model presented above, with shear modulus $\mu=1$, the Poisson ratio $\nu=0.25$ and mass density $\rho=1$, with the PML depth $L_{Pi} \equiv L_P$, and the monomial coefficient $f_{0i} \equiv f_0$ the same in all three directions, subjected to the excitation defined above, and its response characterized by the displacements at the center and at the corner of the excitation. The expected error is computed as the mean of the relative maximum error, given by Equation (38) with $\boldsymbol{u}_p$ and $\boldsymbol{u}_e$ now representing the relevant displacement quantities of the PML and the extended mesh model, respectively. The mean relative error is obtained by averaging the relative error in the center and corner displacements for both vertical and horizontal excitations over four different sets of excitation parameters: (a) $\omega_{\mathrm{f}}=1.5$, $t_{\mathrm{d}}=10$, (b) $\omega_{\mathrm{f}}=2.25$, $t_{\mathrm{d}}=15$, (c) $\omega_{\mathrm{f}}=3.0$, $t_{\mathrm{d}}=10$ and (d) $\omega_{\mathrm{f}}=3.75$, $t_{\mathrm{d}}=15$.

Figure 6 compares the minimum expected relative errors for $p=1$ and 2 for various depths of the PML, characterized by n_P, the number of elements through the depth of the PML. It is seen that for a PML more than four elements deep, there is little significant difference in accuracy between the results for the linear and quadratic attenuation functions; $p=2$ gives slightly more accurate results for depths of 4–7 elements, whereas the situation is reversed for depths of 8–12 elements. Based on these results, the numerical examples in this paper use PMLs that are eight elements deep, with the corresponding minimizing coefficient value of $f_0=9.0$ and $p=1$.

Figure 7 compares the displacements from the PML model and the dashpot model with those from the extended mesh, and Table III compares the relative error in the displacements computed from the two models. Note that the PML and the dashpot models are small: the PML starts at a distance of $0.2b$ from the excitation and is only $0.8b$ deep. The results from the PML model are visually indistinguishable from the extended mesh results, even though the domain is small enough for the dashpots to reflect waves back early in the simulation, as manifested in the higher response amplitudes and larger errors of the results from the dashpot model.

The effect of lumping of the PML matrices and the effect of PML on the critical time step size were also studied. The time step size required for stability of a corresponding fully elastic model also served as a stable time step for the PML model. Use of a consistent formulation led to a negligible decrease in the accuracy of results but a considerably reduced critical time step size. Use of the intermediate lumped formulation resulted in a strong long-time instability in the free-vibration phase even for very small time step sizes.

DOI: 10.1002/nme

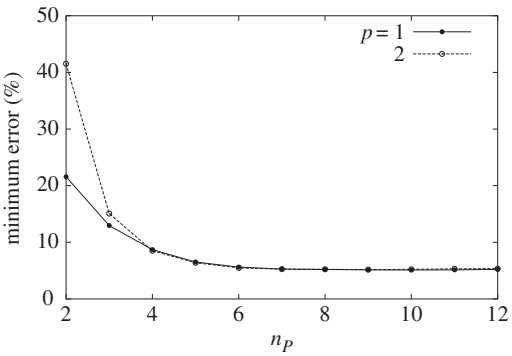

Figure 6. Minimum expected relative error in displacements for different numbers of elements n_P through the depth of the PML in the canonical half-space PML model, for linear and quadratic attenuation functions; $b=1$; $L_e=0.2b$, $L_P=0.1bn_P$; $\mu=1$, $\nu=0.25$, $\rho=1$.

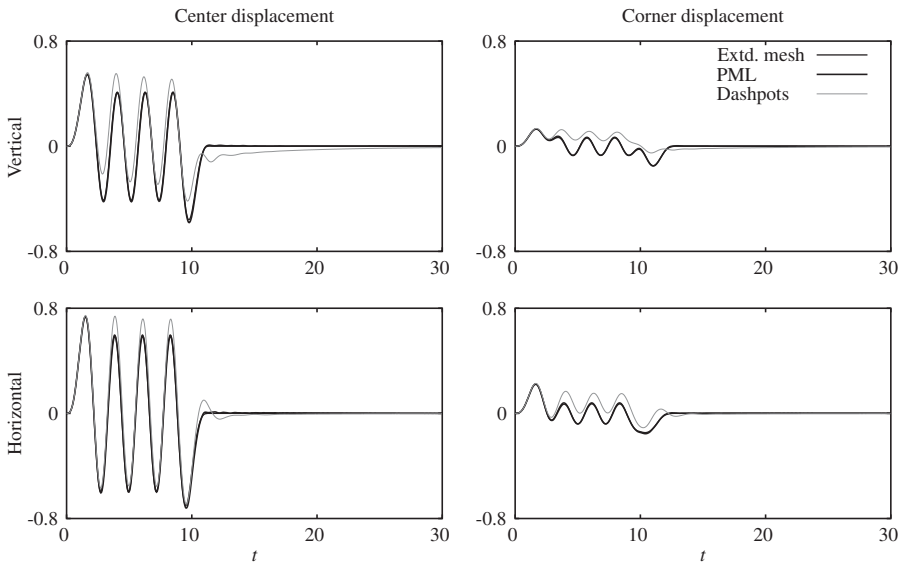

Figure 7. Displacements on the surface of a half-space due to applied forces: vertical displacements due to vertical excitation; horizontal displacements due to horizontal excitation; $b=1$; $L_e=0.2b$, $L_P=0.8b$; $\mu=1$, $\nu=0.25$, $\rho=1$; $t_d=10$, $\omega_f=3.00$. The large errors due to the dashpot model highlight the small size of the domain.

The efficacy of the PML model may be gauged by comparing the computational costs of the three models, as presented in Table IV. Both the PML and the dashpot models have the same number of elements, which is significantly smaller than the number of elements in the extended mesh. However, the time step size required for stability of the dashpot model is smaller than that of a fully elastic model, because the dashpots introduce material damping into the system. Therefore,

DOI: 10.1002/nme

Table III. Relative error in displacements on the surface of a half-space due to applied forces: $b=1$; $L_e=0.2b$, $L_P=0.8b$; $\mu=1$, $v=0.25$, $\rho=1$; $t_d=10$, $\omega_f=3.00$.

		Center displacement		Corner displacement	
	Excitation	PML	Dashpot	PML	Dashpot
% error	Vertical	4.98	45.67	6.07	85.31
	Horizontal	5.79	21.76	5.04	53.24

The large errors due to the dashpot model highlight the small size of the domain.

Table IV. Comparison of computational costs of three models for a half-space.

Model	No. of elements	No. of time steps	Wall-clock time
PML	4000	614	30.2 s
Dashpots	4000	876	14.4 s (1-point elastic) 20.6 s (8-point elastic)
Extended mesh	10 140 000 (V) 15 812 500 (H)	878	35.1 proc-hours (V) 59.3 proc-hours (H)

The dashpot model was discretized using both under-integrated (1-point elastic) and fully integrated (8-point elastic) elastic elements. The mesh size for the extended mesh was different for vertical (V) and horizontal (H) excitations.

the dashpot model required more time steps to complete than the PML model. In order to obtain a realistic assessment of the computational cost, the dashpot model, as well as the elastic region in the PML model, was discretized with under-integrated elements with hourglass control [44] as well as with fully integrated elements; the results from the two formulations were of similar accuracy. The use of under-integrated elastic elements within the PML model did not result in any noticeable reduction in computational cost because the elastic region is much smaller than the PML region. Results for the PML and dashpot models were obtained using the explicit finite element code LS-DYNA [54] on a desktop workstation with a 2.6 GHz AMD Opteron processor, whereas the extended mesh results were obtained using a specially optimized and parallelized in-house code running on 16 processors of a 32-processor node of 1.7 GHz IBM Power4+ processors at the San Diego Supercomputer Center. Although the differing systems make a direct comparison of the wall-clock times difficult, it is remarkable that the PML model achieves the accuracy of the extended mesh model at a cost comparable to the dashpot model, several orders of magnitude smaller than the cost of the extended mesh.

Figure 8(a) shows a quarter model of a layer on a half-space, with a layer of depth d with shear modulus μ_l, supported by a half-space of shear modulus μ_h, and with the Poisson ratio v and mass density ρ in both domains, and Figure 8(b) shows a corresponding PML model. Note that the PML model must incorporate the interface between the layer and the half-space because it is a physical feature that generates wave reflections in the physical unbounded domain model; the PML is meant to eliminate only spurious reflections from the outer boundary. The elastic moduli for the PMLs employed for the layer and the half-space are set to the moduli for the corresponding elastic media. A viscous dashpot model is also employed for comparison, where the entire domain,

DOI: 10.1002/nme

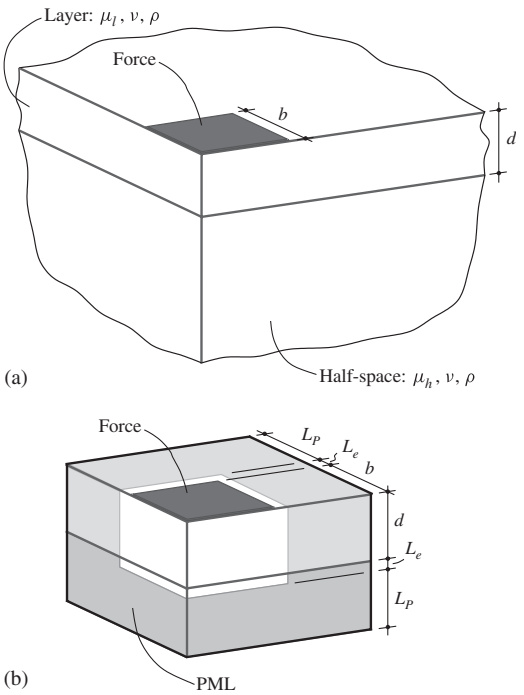

Figure 8. (a) Quarter model of a layer on a half-space subjected to a uniform force applied over a square area of half-width b and (b) a PML model fixed at the outer boundary.

including the PML region, is taken to be elastic, and consistent dashpots model the outer boundary. An extended mesh elastic model with viscous dashpots at the outer boundary—extending laterally to a distance of $20b$ from the center of the excitation for vertical excitation and $25b$ for horizontal, and downward to $35b$ from the base of the layer—is used as a benchmark model.

Figure 9 shows the displacements computed from the three models, and Table V compares the errors due to the PML and the dashpot models. The results from the PML model are virtually indistinguishable from those from the extended mesh, even though the domain is small enough for the dashpot model to generate spurious reflections. The computational cost of the PML model, as shown in Table VI, is of the same order of magnitude as that of the dashpot model, but an insignificant fraction of the cost of the extended mesh model. The critical time step size for the elastic elements was adequate as a stable time step size for the PML elements. Using the consistent formulation of the PML had little effect on the accuracy of results, but reduced the critical time step size considerably. The intermediate lumped formulation showed a strong long-time instability in the free-vibration phase even for very small time step sizes.

Figure 10(a) shows a quarter-model of a layer of depth d on a rigid base, with shear modulus μ, mass density ρ and the Poisson ratio ν, and Figure 10(b) shows its PML model. The corresponding viscous dashpot model is entirely elastic, with consistent dashpots replacing the fixed lateral boundaries. The benchmark extended mesh model extends laterally to $22b$ from the center of the excitation for vertical excitation and $25b$ for horizontal. Figure 11 shows that the PML model produces accurate results even with a small bounded domain where the dashpot model generates

DOI: 10.1002/nme

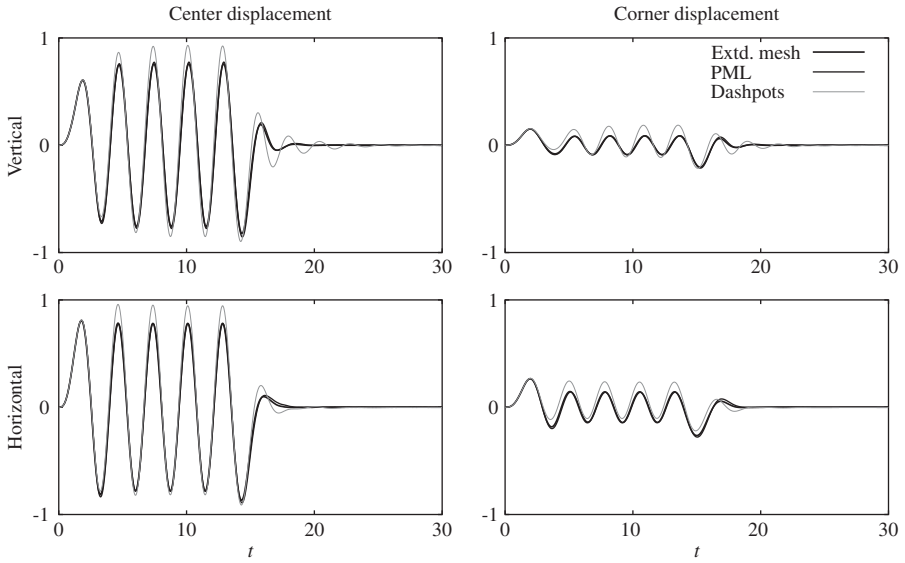

Figure 9. Displacements on the surface of a layer on a half-space due to applied forces: vertical displacements due to vertical excitation; horizontal displacements due to horizontal excitation; $b=1$, $d=b$; $L_e=0.2b$, $L_P=0.8b$; $\mu_l=1$, $\mu_h=2\mu_l$, $\nu=0.25$, $\rho=1$; $t_{\mathrm{d}}=15$, $\omega_{\mathrm{f}}=2.25$. The errors due to the dashpot model highlight the small size of the domain.

Table V. Relative error in displacements on the surface of a layer on a half-space due to applied forces: $b=1$, $d=b$; $L_e=0.2b$, $L_P=0.8b$; $\mu_l=1$, $\mu_h=2\mu_l$, $\nu=0.25$, $\rho=1$; $t_{\mathrm{d}}=15$, $\omega_{\mathrm{f}}=2.25$.

		Center displacement		Corner displacement	
	Excitation	PML	Dashpot	PML	Dashpot
% error	Vertical	6.79	27.88	8.29	51.84
	Horizontal	6.51	20.19	9.75	41.83

The errors due to the dashpot model highlight the small size of the domain.

spurious reflections. The PML model is able to follow the extended mesh result in the free-vibration phase of the displacements from horizontal excitation—in the direction of unboundedness of the domain—when the results from the dashpot model are entirely inadequate; this is reflected in the comparison in Table VII of errors due to either model. The slight phase difference between the PML and the extended mesh results in the free-vibration phase may be due to evanescent waves not being entirely attenuated [36]. Table VIII shows that the PML model is able to achieve this accuracy at a cost that is of the same order of magnitude as that of the dashpot model, and at a small fraction of the cost of the extended mesh model. The effect of lumping of the PML matrices and the effect of PML on the critical time step size were similar to that observed for the half-space and layer-on-half-space models.

DOI: 10.1002/nme

Table VI. Comparison of computational costs of three models for a layer on a half-space.

Model	No. of elements	No. of time steps	Wall-clock time
PML	8000	867	65.6 s (1-point elastic) 67.9 s (8-point elastic)
Dashpots	8000	1237	15.4 s (1-point elastic) 44.3 s (8-point elastic)
Extended mesh	14 584 000 (V) 22 742 500 (H)	1256	116.7 proc-hours (V) 170.5 proc-hours (H)

The dashpot model, as well as the elastic region in the PML model, was discretized using both under-integrated (1-point elastic) and fully integrated (8-point elastic) elastic elements. The mesh size for the extended mesh was different for vertical (V) and horizontal (H) excitations.

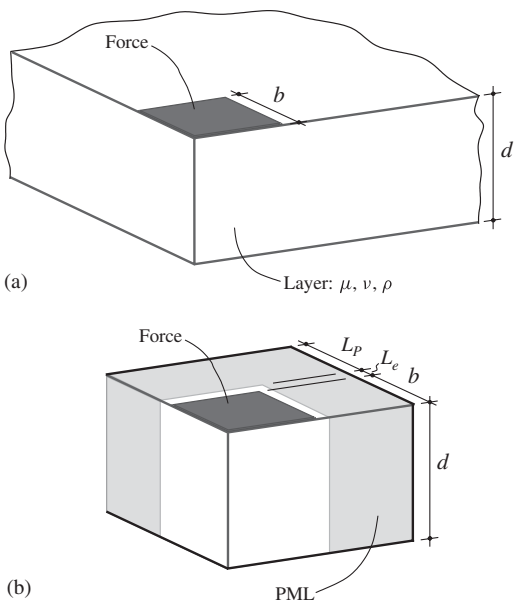

Figure 10. (a) Quarter model of a layer on a rigid base subjected to a uniform force applied over a square area of half-width b and (b) a PML model fixed at the outer boundary.

6. CONCLUSIONS

This paper has presented a three-dimensional PML for transient elastic waves along with its displacement-based finite element implementation, by extending previous work by the author [36]. The initial development is similar to the previous work: a core frequency-domain PML [35] is transformed into the time domain by a convenient choice of the stretching functions, and the time-domain equations are then implemented straightforwardly in a finite element setting. For notational convenience, the development employs a linear elastic material, but PMLs can be formulated for linear visco-elastic materials as well [18, 36].

DOI: 10.1002/nme

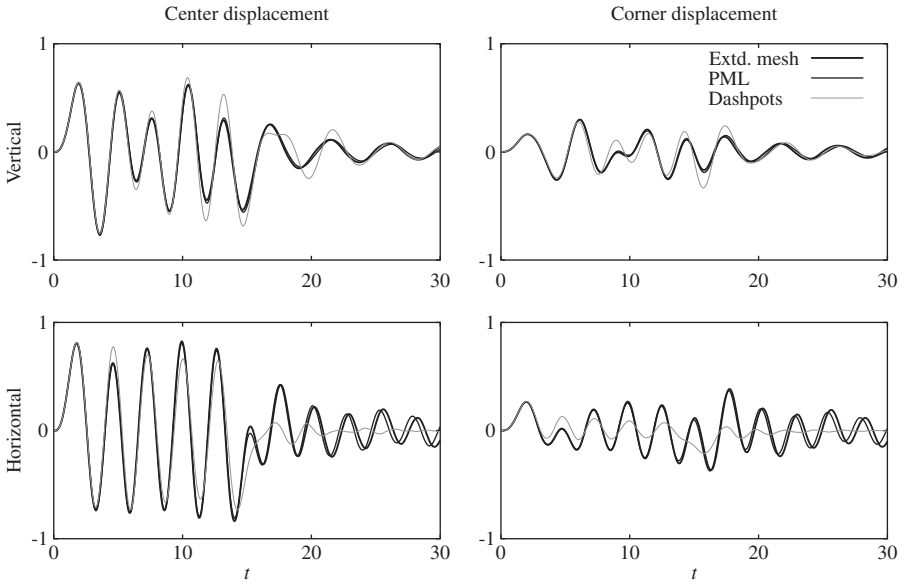

Figure 11. Displacements on the surface of a layer on a rigid base due to applied forces: vertical displacements due to vertical excitation; horizontal displacements due to horizontal excitation; $b=1$, $d=2b$; $L_e=0.2b$, $L_P=0.8b$; $\mu=1$, $\nu=0.25$, $\rho=1$; $t_d=15$, $\omega_f=2.25$. The large errors due to the dashpot model highlight the small size of the domain.

Table VII. Relative error in displacements on the surface of a layer on a rigid base due to applied forces: $b=1$, $d=2b$; $L_e=0.2b$, $L_P=0.8b$; $\mu=1$, $\nu=0.25$, $\rho=1$; $t_d=15$, $\omega_f=2.25$.

		Center displacement		Corner displacement	
	Excitation	PML	Dashpot	PML	Dashpot
% error	Vertical	6.67	31.81	11.25	56.62
	Horizontal	15.00	48.30	30.85	94.86

The large errors due to the dashpot model highlight the small size of the domain.

The novel contribution of this paper over the previous work is in making the displacement-based PML suitable for explicit time integration, thus making it practicable for use in large-scale three-dimensional dynamic analyses. The two-dimensional elastic PML in Reference [36] resulted in an unsymmetric stiffness matrix and employed implicit time integration, thereby incurring the expense of solving unsymmetric equations at each time step. To take advantage of the lack of this overhead in explicit integration, this paper presents an efficient method for computing the strain terms in the PML, by exploiting the property that the matrices of the PML attenuation functions are diagonal in the characteristic basis of the PML.

The viability of using explicit integration with this PML formulation was investigated by studying (a) the effect of PML on the critical time step size and (b) the effect of lumping of inertial matrices in the PML on the accuracy of results as well as on the critical time step size,

DOI: 10.1002/nme

Table VIII. Comparison of computational costs of three models for a layer on a rigid base.

Model	No. of elements	No. of time steps	Wall-clock time
PML	8000	614	45.3 s (1-point elastic) 50.5 s (8-point elastic)
Dashpots	8000	828	10.5 s (1-point elastic) 31.9 s (8-point elastic)
Extended mesh	976 800 (V) 1 260 000 (H)	812	4.7 proc-hours (V) 5.9 proc-hours (H)

The dashpot model, as well as the elastic region in the PML model, was discretized using both under-integrated (1-point elastic) and fully integrated (8-point elastic) elastic elements. The mesh size for the extended mesh was different for vertical (V) and horizontal (H) excitations.

in the context of a model semi-infinite bar. It was found that the PML does not affect the critical time step size significantly. The consistent formulation of the PML gave results that were marginally more accurate than the lumped formulation; this seemed to go against the conclusion of earlier analyses that lumped matrices are better matched with explicit integration than are consistent matrices [45, 52]. However, it was felt that the difference in accuracy of the two formulations was too small to warrant further investigation of this discrepancy with established results. Furthermore, it was observed that the consistent formulation of the PML yielded significantly smaller critical time step sizes than the lumped formulation, in keeping with behavior well known for elastic elements [45]. The intermediate formulation of the PML—where only the mass matrix is lumped and other inertial matrices are consistent—exhibited a strong long-time instability in the free-vibration phase under longitudinal excitation irrespective of the time step size.

The PML formulation was used to model the classical soil–structure interaction problems of a square flexible footing on a (i) half-space, (ii) layer on a half-space and (iii) layer on a rigid base. Optimal values of the PML depth and attenuation function were found by minimizing the error in the response of a canonical half-space PML model over a range of these PML parameters. Both quadratic and linear attenuation functions were considered, and it was found that for a PML more than four elements deep, there was little significant difference in accuracy between the two. Based on this study, the PMLs for these classical problems were chosen to be eight elements deep, with the corresponding optimal attenuation functions. The PML models gave highly accurate results, even though the domains were small enough that comparably sized viscous dashpot models generated spurious wave reflections early on in the duration of the simulation. The computational cost of the PML models was comparable to that of the dashpot models, but was an insignificant fraction of the cost of the corresponding extended mesh models used as benchmarks.

The effect of lumping of the PML matrices and the effect of PML on the critical time step size for these classical problems were similar to those observed for the semi-infinite bar. It was found that the critical time step size for elastic elements served as a stable time step size for the PML elements and that using a consistent formulation of the PML had a negligible effect on the accuracy of results but reduced the critical time step size significantly. The intermediate formulation of the PML exhibited a strong long-time instability in the free-vibration phase even for very small time steps. Because consistent matrices reduce the critical time step size, it is speculated that this instability arises because the specific combination of lumped and consistent matrices reduce

DOI: 10.1002/nme

the critical step size to an unreasonably small value; if correct, this observation could provide an alternate explanation of the long-time instability observed in some PML formulations [55, 56].

It has been verified numerically that this PML model is stable not only in the long time in free vibration, but even if it is excited over a long duration. Although this formulation uses an isotropic material, its long-time stability suggests that it may be worthwhile to investigate its stability in the presence of an anisotropic elastic material, where other PML formulations have exhibited instabilities [31, 40].

NOMENCLATURE

a_0	non-dimensional frequency
b	half-width of footing
$\tilde{\mathbf{B}}^{\mathrm{ee}}$, $\tilde{\mathbf{B}}^{\mathrm{ep}}$, $\tilde{\mathbf{B}}^{\mathrm{pp}}$	compatibility matrices
c_{s}	shear wave speed
$\mathbf{c}^e$, $\mathbf{c}$	element-level and global inertial damping matrices
$\mathbf{C}$, C_{ijkl}	material stiffness tensor
d	depth of the layer
$\boldsymbol{d}$	nodal displacements
$\mathbf{D}$	material moduli matrix
$\mathscr{D}$	time integral of $\boldsymbol{d}$
$\{\boldsymbol{e}_i\}$, $\{\boldsymbol{e}'_i\}$	standard orthonormal basis and PML basis
$\mathbf{E}$, $\hat{\mathbf{E}}$	time integral of $\boldsymbol{\varepsilon}$, $\hat{\boldsymbol{\varepsilon}}$
f_0	coefficient of monomial in f_i^{e}, f_i^{p}
f_{M}, f_{C}, f_{K}, f_{H}	see Equation (13)
f_i^{e}, f_i^{p}	attenuation functions
$\mathbf{F}^{\mathrm{e}}$, $\mathbf{F}^{\mathrm{p}}$, $\tilde{\mathbf{F}}^{\mathrm{ee}}$, $\tilde{\mathbf{F}}^{\mathrm{ep}}$, $\tilde{\mathbf{F}}^{\mathrm{pp}}$	attenuation tensors; Equations (7), (10)
$\mathrm{i}=\sqrt{-1}$	unit imaginary number
$\mathscr{J}$	Jacobian determinant of coordinate stretch
$\mathbf{k}^e$, $\mathbf{k}$	element-level and global inertial stiffness matrices
$\mathbf{K}^e$, $\mathbf{K}$	element-level and global inertial coefficient matrices
L	characteristic length of the system
L_e	depth of the elastic region
L_P, L_{Pi}	depth of PML
$\mathbf{m}^e$, $\mathbf{m}$	element-level and global mass matrices
n_P	number of elements through depth of PML
$\boldsymbol{n}$	unit normal to a surface
$\mathbf{N}$, $\mathbf{N}_d$, N_I	(arrays of) nodal shape functions
$\boldsymbol{p}^e_{\mathrm{int}}$, $\boldsymbol{p}_{\mathrm{int}}$, $\boldsymbol{p}_{\mathrm{ext}}$	internal and external force terms
$\mathbf{Q}$, Q_{ij}	rotation-of-basis matrix
t_{d}	duration of applied force
$\boldsymbol{u}$	displacements
$\boldsymbol{U}$	time integral of $\boldsymbol{u}$
$\boldsymbol{w}$	arbitrary weighting function in a weak form
x_i, x'_i, $\boldsymbol{x}$	coordinates

DOI: 10.1002/nme

Greek symbols

δ_{ij}	Kronecker delta
Δt	time step size
ε_{ij}, $\boldsymbol{\varepsilon}$, $\hat{\boldsymbol{\varepsilon}}$	strain quantities in global basis
ε'_{ij}, $\boldsymbol{\varepsilon}'$	strain quantities in PML basis
κ	bulk modulus
λ_i	complex coordinate-stretching function
$\boldsymbol{\Lambda}$	stretch tensor
μ	shear modulus
ν	the Poisson ratio
ρ	mass density
$\boldsymbol{\sigma}$, $\hat{\boldsymbol{\sigma}}$	stress quantities
$\boldsymbol{\Sigma}$, $\hat{\boldsymbol{\Sigma}}$	time integral of $\boldsymbol{\sigma}$, $\hat{\boldsymbol{\sigma}}$
$\tilde{\boldsymbol{\Sigma}}$, $\hat{\tilde{\boldsymbol{\Sigma}}}$	time integral of $\boldsymbol{\Sigma}$, $\hat{\boldsymbol{\Sigma}}$
ω	excitation frequency
ω_{f}	dominant forcing frequency of applied force
$\boldsymbol{\Omega}$	entire PML domain
$\boldsymbol{\Omega}^e$	element domain

ACKNOWLEDGEMENTS

The initial development of this formulation was carried out by the author while working as a postdoctoral researcher at the University of California, Berkeley, on a project on developing PML toward use in the earthquake analysis of concrete dams, under Award No. W912HZ-05-P-0128 to Prof. Anil K. Chopra from the U.S. Bureau of Reclamation and from the Army Corps of Engineers, with project liaisons Larry Nuss at USBR and Robert Hall at the Army Corps; this financial support is gratefully acknowledged. This research was supported in part by the National Science Foundation through the San Diego Supercomputer Center under the Academic Associates Program and utilized the p690 nodes on the Datastar system. The author would like to thank the following people for their helpful advice and comments during the course of this study: Anil Chopra, Bob Taylor, John Hallquist, Prashanth Vijalapura, Jerome Solberg, David Bindel, Grant Cook and Brian Wainscott. The author would also like to thank the anonymous reviewers whose comments helped improve this paper.

REFERENCES

1. Givoli D. *Numerical Methods for Problems in Infinite Domains*. Elsevier: Amsterdam, 1992.
2. Tsynkov SV. Numerical solution of problems on unbounded domains. A review. *Applied Numerical Mathematics* 1998; **27**(4):465–532.
3. Lysmer J, Kuhlemeyer RL. Finite dynamic model for infinite media. *Journal of the Engineering Mechanics Division* (ASCE) 1969; **95**(EM4):859–877.
4. Clayton R, Engquist B. Absorbing boundary conditions for acoustic and elastic wave equations. *Bulletin of the Seismological Society of America* 1977; **67**(6):1529–1540.
5. Higdon RL. Absorbing boundary conditions for elastic waves. *Geophysics* 1991; **56**(2):231–241.
6. Manolis GD, Beskos DE. *Boundary Element Methods in Elastodynamics*. Unwin Hyman: London, 1988.
7. Givoli D, Keller JB. Non-reflecting boundary conditions for elastic waves. *Wave Motion* 1990; **12**(3):261–279.
8. Givoli D, Vigdergauz S. Artificial boundary conditions for 2D problems in geophysics. *Computer Methods in Applied Mechanics and Engineering* 1993; **110**(1–2):87–101.
9. Song C, Wolf JP. The scaled boundary finite-element method—alias consistent infinitesimal finite-element cell method—for elastodynamics. *Computer Methods in Applied Mechanics and Engineering* 1997; **147**(3–4):329–355.

DOI: 10.1002/nme

10. Guddati MN, Tassoulas JL. Continued-fraction absorbing boundary conditions for the wave equation. *Journal of Computational Acoustics* 2000; **8**(1):139–156.
11. Givoli D. High-order nonreflecting boundary conditions without high-order derivatives. *Journal of Computational Physics* 2001; **170**(2):849–870.
12. Givoli D. High-order local non-reflecting boundary conditions: a review. *Wave Motion* 2004; **39**(4):319–326.
13. Hagstrom T, Warburton T. A new auxiliary variable formulation of high-order local radiation boundary conditions: corner compatibility conditions and extensions to first-order systems. *Wave Motion* 2004; **39**(4):327–338.
14. Givoli D, Hagstrom T, Patlashenko I. Finite element formulation with high-order absorbing boundary conditions for time-dependent waves. *Computer Methods in Applied Mechanics and Engineering* 2006; **195**(29–32):3666–3690.
15. Bérenger JP. A perfectly matched layer for the absorption of electromagnetic waves. *Journal of Computational Physics* 1994; **114**(2):185–200.
16. Chew WC, Weedon WH. A 3D perfectly matched medium from modified Maxwell's equations with stretched coordinates. *Microwave and Optical Technology Letters* 1994; **7**(13):599–604.
17. Taflove A, Hagness SC. *Computational Electrodynamics*: *The Finite-difference Time-domain Method* (3rd edn). Artech House Publishers: Norwood, MA, 2005.
18. Teixeira FL, Chew WC. Unified analysis of perfectly matched layers using differential forms. *Microwave and Optical Technology Letters* 1999; **20**(2):124–126.
19. Qi Q, Geers TL. Evaluation of the perfectly matched layer for computational acoustics. *Journal of Computational Physics* 1998; **139**(1):166–183.
20. Turkel E, Yefet A. Absorbing PML boundary layers for wave-like equations. *Applied Numerical Mathematics* 1998; **27**(4):533–557.
21. Harari I, Slavutin M, Turkel E. Analytical and numerical studies of a finite element PML for the Helmholtz equation. *Journal of Computational Acoustics* 2000; **8**(1):121–137.
22. Hu FQ. On absorbing boundary conditions for linearized Euler equations by a perfectly matched layer. *Journal of Computational Physics* 1996; **129**(1):201–219.
23. Zeng YQ, He JQ, Liu QH. The application of the perfectly matched layer in numerical modeling of wave propagation in poroelastic media. *Geophysics* 2001; **66**(4):1258–1266.
24. Chew WC, Liu QH. Perfectly matched layers for elastodynamics: a new absorbing boundary condition. *Journal of Computational Acoustics* 1996; **4**(4):341–359.
25. Hastings FD, Schneider JB, Broschat SL. Application of the perfectly matched layer (PML) absorbing boundary condition to elastic wave propagation. *Journal of the Acoustical Society of America* 1996; **100**(5):3061–3069.
26. Zhang YG, Ballmann J. Two techniques for the absorption of elastic waves using an artificial transition layer. *Wave Motion* 1997; **25**(1):15–33.
27. Liu QH. Perfectly matched layers for elastic waves in cylindrical and spherical coordinates. *Journal of the Acoustical Society of America* 1999; **105**(4):2075–2084.
28. Bécache E, Joly P, Tsogka C. Fictitious domains, mixed finite elements and perfectly matched layers for 2-D elastic wave propagation. *Journal of Computational Acoustics* 2001; **9**(3):1175–1201.
29. Collino F, Tsogka C. Application of the perfectly matched absorbing layer model to the linear elastodynamic problem in anisotropic heterogeneous media. *Geophysics* 2001; **66**(1):294–307.
30. Marcinkovich C, Olsen K. On the implementation of perfectly matched layers in a three-dimensional fourth-order velocity–stress finite difference scheme. *Journal of Geophysical Research* 2003; **108**(B5):2276.
31. Bécache E, Fauqueux S, Joly P. Stability of perfectly matched layers, group velocities and anisotropic waves. *Journal of Computational Physics* 2003; **188**(2):399–433.
32. Festa G, Nielsen S. PML absorbing boundaries. *Bulletin of the Seismological Society of America* 2003; **93**(2): 891–903.
33. Komatitsch D, Tromp J. A perfectly matched layer absorbing boundary condition for the second-order seismic wave equation. *Geophysical Journal International* 2003; **154**(1):146–153.
34. Wang T, Tang X. Finite-difference modeling of elastic wave propagation: a nonsplitting perfectly matched layer approach. *Geophysics* 2003; **68**(5):1749–1755.
35. Basu U, Chopra AK. Perfectly matched layers for time-harmonic elastodynamics of unbounded domains: theory and finite-element implementation. *Computer Methods in Applied Mechanics and Engineering* 2003; **192**(11–12): 1337–1375.
36. Basu U, Chopra AK. Perfectly matched layers for transient elastodynamics of unbounded domains. *International Journal for Numerical Methods in Engineering* 2004; **59**(8):1039–1074. Erratum: *International Journal for Numerical Methods in Engineering* 2004; **61**(1):156–157.

DOI: 10.1002/nme

37. Cohen G, Fauqueux S. Mixed spectral finite elements for the linear elasticity system in unbounded domains. *SIAM Journal on Scientific Computing* 2005; **26**(3):864–884.
38. Festa G, Vilotte JP. The Newmark scheme as velocity–stress time-staggering: an efficient PML implementation for spectral element simulations of elastodynamics. *Geophysical Journal International* 2005; **161**(3):789–812.
39. Harari I, Albocher U. Studies of FE/PML for exterior problems of time-harmonic elastic waves. *Computer Methods in Applied Mechanics and Engineering* 2006; **195**(29–32):3854–3879.
40. Appelö D, Kreiss G. A new absorbing layer for elastic waves. *Journal of Computational Physics* 2006; **215**(2):642–660.
41. Ma S, Liu P. Modeling of the perfectly matched layer absorbing boundaries and intrinsic attenuation in explicit finite-element methods. *Bulletin of the Seismological Society of America* 2006; **96**(5):1779–1794.
42. Komatitsch D, Martin R. An unsplit convolutional perfectly matched layer improved at grazing incidence for the seismic wave equation. *Geophysics* 2007; **72**(5):SM155–SM167.
43. Zienkiewicz OC, Taylor RL, Zhu JZ. *The Finite Element Method*: *Its Basis and Fundamentals* (6th edn). Elsevier Butterworth-Heinemann: London, 2005.
44. Belytschko T, Liu WK, Moran B. *Nonlinear Finite Elements for Continua and Structures*. Wiley: New York, 2000.
45. Hughes TJR. *The Finite Element Method*: *Linear Static and Dynamic Finite Element Analysis*. Dover: New York, NY, 2000.
46. Wolf JP. *Soil-Structure-Interaction Analysis in Time Domain*. Prentice-Hall: Englewood Cliffs, NJ, 1988.
47. Bao H, Bielak J, Ghattas O, Kallivokas LF, O'Hallaron DR, Shewchuck JR, Xu J. Large-scale simulation of elastic wave propagation in heterogeneous media on parallel computers. *Computer Methods in Applied Mechanics and Engineering* 1998; **152**(1–2):85–102.
48. Bindel DS, Govindjee S. Elastic PMLs for resonator anchor loss simulation. *International Journal for Numerical Methods in Engineering* 2005; **64**(6):789–818.
49. Cerjan C, Kosloff D, Kosloff R, Reshef M. A nonreflecting boundary-condition for discrete acoustic and elastic wave-equations. *Geophysics* 1985; **50**(4):705–708.
50. Sochaki J, Kubichek R, George J, Fletcher WR, Smithson S. Absorbing boundary conditions and surface waves. *Geophysics* 1987; **52**(1):60–71.
51. Zhao L, Cangellaris AC. A general approach for the development of unsplit-field time-domain implementations of perfectly matched layers for FDTD grid truncation. *IEEE Microwave and Guided Wave Letters* 1996; **6**(5): 209–211.
52. Krieg RD, Key SW. Transient shell response by numerical time integration. *International Journal for Numerical Methods in Engineering* 1973; **7**(3):242–411.
53. Collino F, Monk PB. Optimizing the perfectly matched layer. *Computer Methods in Applied Mechanics and Engineering* 1998; **164**(1):157–171.
54. Hallquist JO. *LS-DYNA Keyword User's Manual*, *Version 971*. Livermore Software Technology Corporation: Livermore, CA, 2007.
55. Abarbanel S, Gottlieb D, Hesthaven JS. Long time behavior of the perfectly matched layer equations in computational electromagnetics. *Journal of Scientific Computing* 2002; **17**(1–4):405–422.
56. Bécache E, Petropoulos G, Gedney SD. On the long-time behavior of unsplit perfectly matched layers. *IEEE Transactions on Antennas and Propagation* 2004; **52**(5):1335–1342.

DOI: 10.1002/nme